Structure and morphology of epitaxial $PbZrO_3$ films grown by metalorganic chemical vapor deposition

M. P. Moret[a] and J. J. Schermer
University of Nijmegen, Research Institute for Materials, Toernooiveld 1, 6525 ED Nijmegen, The Netherlands

F. D. Tichelaar
National Center for HREM, Rotterdamseweg 137, 2628 AL Delft, The Netherlands

E. Aret and P. R. Hageman
University of Nijmegen, Research Institute for Materials, Toernooiveld 1, 6525 ED Nijmegen, The Netherlands

(Received 19 April 2002; accepted for publication 15 July 2002)

$PbZrO_3$ (PZ) films of different thicknesses have been grown by metalorganic chemical vapor deposition on $SrTiO_3$ (STO) substrates. The structure of the films was determined by x-ray diffraction and transmission electron microscopy. At the deposition temperature, the growth is cube on cube and is therefore heteroepitaxial. During cool down, PZ goes through a phase transformation from paraelectric to antiferroelectric at the Curie temperature and its cubic structure is stretched to orthorhombic. This results in domain formation in the PZ films corresponding to the different stretching directions. At room temperature, the thin PZ film consists of at least two different (120) domain variants and the thin-film–substrate relation can be described as (120)[002]PZ//(100) $[00\bar{1}]$ STO for one of these variants. By etching down a thick film, it was observed that ~260 nm is the threshold thickness, above which two additional different (002) domain variants appear in addition to the (120) domain variants. For one of the (002) domain variants, the thin-film–substrate relation can be described as (002)[100]PZ//(100)[011] STO. The surface morphology of the thick films, studied by scanning electron and atomic force microscopy, is partly covered with pyramids. These pyramids can originate from both (120) or (002) domains and are due to a higher growth rate of these two planes compared to the rest of the layer. A suggestion is made for pyramid-facet indexing for both domains. © *2002 American Institute of Physics.* [DOI: 10.1063/1.1505993]

I. INTRODUCTION

$PbZr_xTi_{1-x}O_3$ (PZT), ferroelectric (FE) at room temperature, is a solid solution from $PbZrO_3$ (PZ) and $PbTiO_3$ (PT), where x is the ratio defined by the amount of Zr in the compound: $x=[Zr]/[Zr+Ti]$.[1] PZT thin films are candidates for several applications such as memories,[2] piezoelectric devices,[3] and electro-optic devices.[4] Of particular interest are the materials with compositions around the morphotropic phase boundary ($x=0.53$), as they show high piezoelectric effects and dielectric constants. PZ ($x=1$) is antiferroelectric (AFE) and has received significantly less attention. Its AFE phase can be switched to the FE phase by applying an electric field[5,6] and the relatively large strain increase accompanying this phase change could be used in devices requiring on/off strain states.[5,6] For these applications, PZ thin films seem more interesting than bulk materials as they have higher breakdown strength. In addition to phase switching, other applications related to PZ electro-optical properties are reported in literature.[7]

FE/AFE films are usually grown above the Curie temperature, at which the AFE or FE phase transforms to paraelectric. Therefore, the heteroepitaxial growth of ferroelectric material leads to the formation of domains during cool down after deposition. This phenomenon has been investigated for tetragonal PT and PZT[8–11] as well as for rhombohedral PZT,[12,13] but not for orthorhombic PZ. The growth of polycrystalline PZ films on platinized substrates by different techniques (magnetron sputtering, sol–gel, laser ablation) and their electrical properties have been reported.[5,6,14,15] Although some applications, such as electro-optical applications, might require epitaxial films (single crystals) as they have a higher potential than poled polycrystalline structures,[16] no investigations on epitaxially deposited PZ films were encountered. In this article, we present data on the structure and morphology of thin and thick PZ films heteroepitaxially deposited on $SrTiO_3$ (STO) substrates. The structure of these films, measured by x-ray diffraction (XRD), are compared and related to the transmission electron microscopy (TEM) cross section results and film surface morphology. These observations are further discussed in relation to the processes that occur during growth and cool down.

II. EXPERIMENT

The PZ films were grown by metalorganic chemical vapor deposition (MOCVD) in a cold wall horizontal flow reactor equipped with a rotating disk susceptor and an infrared-lamp heating system. Commercially available tetraethyllead (Mochem Gmbh, Marburg, Germany) and zirconium tetra-*t*-

[a]Electronic mail: mona@sci.kun.nl

TABLE I. MOCVD growth conditions for the PZ films.

Parameter	
Substrate temperature	700 °C
Reactor pressure	5–10 mbar
Lead precursor $[Pb(C_2H_5)_4]$	80 μmol/min
Zirconium precursor $Zr[OC(CH_3)_3]_4$	80 μmol/min
Oxygen flow	60 mmol/min
Total flow through reactor	3000 sccm
Growth time thin films	60 min
Growth time thick films	300 min

butoxide (Inorgtech Ltd, Mildenhall, UK) were used as organometal precursors. Oxygen was used as oxidizing agent and nitrogen as carrier gas. Growth conditions are summarized in Table I. The thin PZ film was obtained in a deposition run of 60 min while seven and two thick films were obtained successively in two separate deposition runs of 300 min. STO crystals (Escete B.V., Enschede, The Netherlands), 0.5 mm thick, (100) oriented within $\pm 0.5°$, were used as substrates. The substrate surface dimensions were 20 mm in diameter for the thin film and 1 by 1 cm for the thick films. The substrates were cleaned successively in acetone, isopropanol, and demineralized water prior to growth.

The structure of the PZ films was investigated by XRD using a powder Philips PW1820 diffractometer with a Cu target ($\lambda = 1.540\,60$ Å) for the θ–2θ spectra. A Bruker D8 Discovery x-ray diffractometer with a Cu target ($\lambda = 1.540\,60$ Å) and a four-bounce monochromator Ge (022) was used to obtain x-ray reflectivity data, rocking curves, and pole figures. The XRD scans were adjusted on the STO (200) peak. The surface morphology of the PZ films was investigated with a JEOL JSM 6330F field-emission scanning electron microscope (SEM) and a Digital Instruments Dimension 3100 Atomic Force Microscope (AFM) in contact mode. The cross section of a thick PZ film was examined using a CM30T and a CM30UT Philips TEM. The composition analyzed by energy dispersive spectroscopy (EDS) in the TEM was compared to the surface composition measured by x-ray fluorescence (XRF) on a similar sample. XRF was performed using an Rh-2400 spectrometer with a 5 mm spot size. The thicknesses of the films were estimated by ellipsometry[17] and confirmed by TEM cross sections for the thick films and by x-ray reflectivity for the thin film. One thick PZ film was dry etched four times to perform a depth analysis by XRD of the layer. The etching was performed in an Alcatel GIR300 at 50 W at a pressure of 5 mTorr with a SF_6 flow of 15 ml/min resulting in an average etch rate of 20 nm/min.

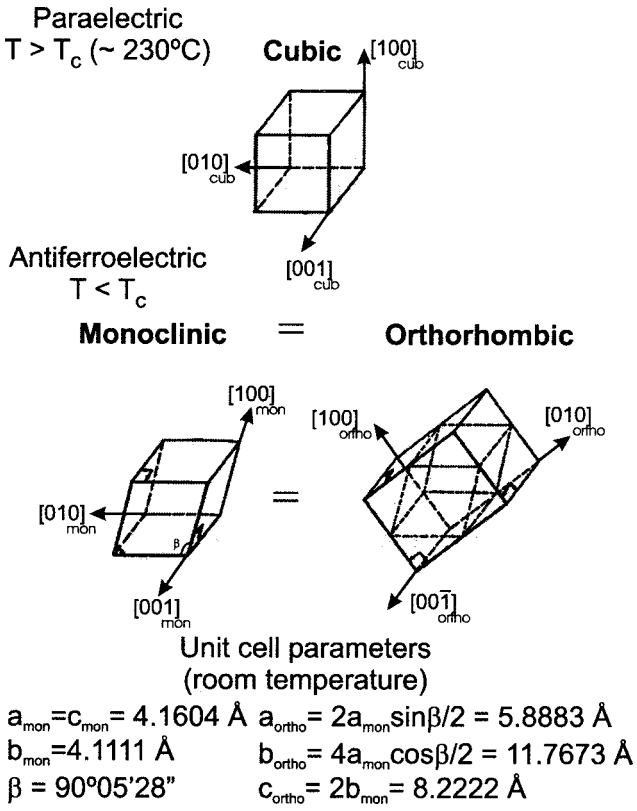

FIG. 1. Schematic representation (not on scale) of the unit cell transformation of PZ from a cubic to an orthorhombic structure with the relationships between the cell parameters of the different symmetry (see Ref. 1).

III. RESULTS AND DISCUSSION

A. $PbZrO_3$ material properties

Above the Curie temperature, around 230 °C, PZ is paraelectric with a cubic structure and below it is AFE with an orthorhombic structure. A schematic representation of the corresponding unit cells is shown in Fig. 1. Upon cooling, cubic PZ is deformed by stretching the cubic structure along $\langle 110 \rangle$. The stretch along the $\langle 110 \rangle$ induces a small angle difference of $5'28''$ with respect to the original unit-cell structure (Fig. 1). The distortion of the cube leads to a monoclinic cell, which can be described more conveniently as an

TABLE II. Growth rates, layer thickness, roughnesses, and composition ([Pb]/[Zr]) of the MOCVD PZ films investigated.

PZ film	Growth rate (nm/min)	Thickness (nm)	Roughness rms (nm)	XRF surface composition	EDS (TEM) average composition (across thickness)	Ellipsometry average surface composition[a]
Thin film	1.75±0.08	105±5	0.59	···	···	≈1.0
Thick films	4.3±0.2	1292±66	30–50	0.90±0.05	0.80±0.10	≈1.0

[a]See Ref. 17.

orthorhombic unit cell. AFE materials have a zero-net polarization as they contain ion chains displaced in one direction with adjacent ion chains displaced in the other direction, leading to a large unit cell containing eight chemical units. For clarity, the films studied in this work will be described starting from the unit-cell axes, as shown in the orthorhombic unit cell in Fig. 1.

B. Samples

In Table II, data with respect to the composition, thickness, and surface roughness of the PZ films are summarized. The difference in growth rates for the thin and the thick films will be discussed later. The XRF, the EDS, and previous ellipsometry analyses of these PZ films[17] indicate that the ratio [Pb]/[Zr] in the film was relatively close to 1 as expected for a perovskite. The EDS measurements are less accurate than the XRF ones as the TEM sample thickness is not exactly known. The ratio [Pb]/[Zr] did not vary from the interface to the surface as measured by EDS in the TEM cross section. This indicates that the growth environment was successfully kept constant during the 300 min growth run. By measuring the weight of the films prior to and after growth and using the thickness determined by ellipsometry and cross section TEM, an average density of the PZ films was estimated as $\rho = 9.1 \pm 0.5$ g/cm^3, which is relatively high compared to 6.98 g/cm^3 for PZT ($x = 0.98$) sintered ceramics.[18] This difference might be due to the fact that our estimated density is for fully continuous crystalline MOCVD films, which are denser than ceramics.

C. Structure

The XRD patterns of the films are shown in Fig. 2. The PZ spectra were indexed according to orthorhombic PZ at room temperature.[18,19] For the thin PZ film on STO, Fig. 2(a) only the orientation (120) is seen. In contrast, for films roughly ten times thicker deposited on similar STO substrates, two orientations, (002) and (120), can be identified [Fig. 2(b)]. The peak positions are listed in Table III. The peaks observed in the thin film are not split as the peaks observed in the thick films, but they are quite broad. The full width at half maximum (FWHM) of the two high intensity (240) peaks from the thick films are respectively 0.05° and 0.06°, and the FWHM of the (240) peak of the thin film is of 0.2° and hides an eventual peak splitting, as will be discussed later.

One of the thick PZ films was successively dry etched four times and the XRD 2θ spectrum of the etched film was measured after each etch step. The film thickness was estimated by weighting the film prior to and after etching and using the estimated PZ density. The XRD spectra are shown in Figs. 2(c)–2(f). The intensity of the {002}-related peaks as well as the {120} splitting progressively decreased and nearly disappeared at the last etch step for a film thickness of about 260 nm. The {120}-related peaks are not clearly visible in Fig. 2(f), but low intensity peaks can still be distinguished as shoulder peaks from the {002}-related peaks. Such weak shoulder peaks are not visible for the 100 nm thin film but, as its XRD spectra and that of the 1420 nm thick PZ film etched down to 260 nm are similar, it indicates that 260 nm is roughly the threshold thickness for the formation of (002) domains.

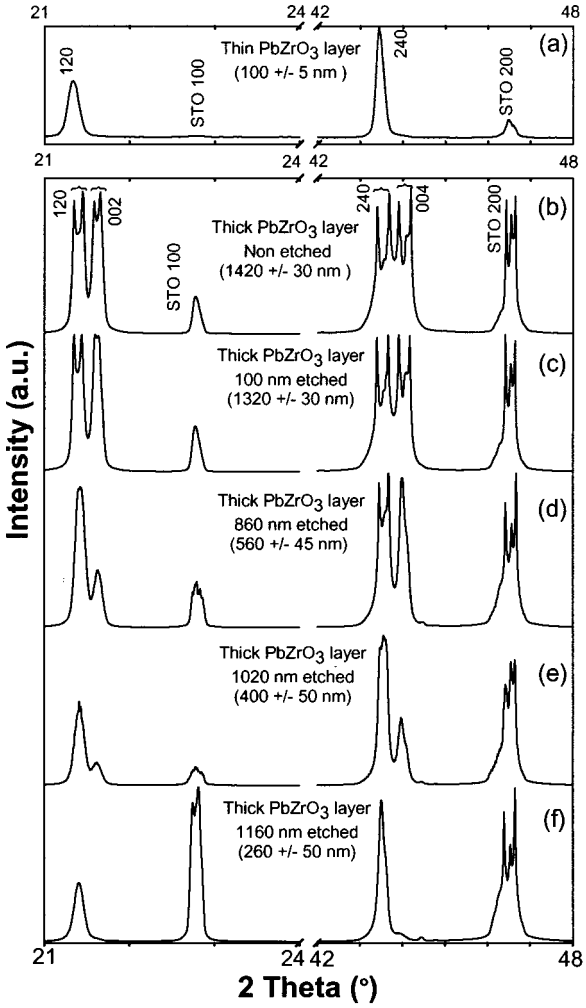

FIG. 2. XRD spectra (θ–2θ scan) of (a) a thin PZ film on STO and (b) a thick PZ film on STO. (c)–(f) the thick film was dry etched four times and the XRD were successively measured. As the film becomes thinner, the {002} peaks disappeared and only one peak for {120} planes survives.

All thick PZ films displayed the same features in the in-plane XRD spectra. There are two observable orientations, (120) and (002), each with multiple splitting. Both (120) and (002) consist of two peaks whereas (240) and (004) consist each of two high-intensity peaks separated by two [and eventually three, although not visible on the displayed spectrum in Fig. 2(b)] lower-intensity peaks with varying intensity from film to film. The high-intensity (120) or (002) peaks do not correspond directly to the respective (240) and (004) high-intensity peaks as seen from the peak position in Table III but to lower-intensity peaks between each (240) and (004) high-intensity-peak pairs. The STO peaks in the XRD spectra shown in Fig. 2 also displayed similar type of peak splitting. Additionally, STO crystals identical to the substrates used for this study, also show splitting in θ–2θ spectra and rocking curves from these peaks indicate a kind of mosaic structure in the STO substrate. Pole figures measurements, performed with a monochromator to avoid eventual peaks originating from Cu $K\alpha_2$, around the symmetric (240) peak confirmed

TABLE III. Position of the 2θ peaks in the PZ films on STO and the Inorganic Crystal Structure Database.[19]

		MOCVD $PbZrO_3$ films			
Reference Powder data ICSD 75-1607		100 nm thick	1450 nm thick		1450 nm thick etched down to 260 nm
2θ	(hkl)	2θ	2θ min	2θ max	2θ
21.339	(120)	21.30	21.35	21.44	21.40
21.605	(002)	···	21.58	21.65	···
43.466	(240)	43.41	43.40	43.68	43.50
44.029	(400)	···	43.90	44.19	

that there are clearly two to three tilts as shown in Figs. 3(a)–3(c). The peak splitting observed in the θ–2θ spectra correspond to these tilts in the pole figures. Though the θ–2θ spectra in Fig. 2(a) from the thin film indicate a single (240) peak in the film, the pole figure shows that there are actually two (240) tilts in the thin film causing the relatively large FWHM of the peak. A similar multitilt structure was found for the (004) peak in the thick PZ film [Fig. 3(d)]. The tilts observed in the pole figure do not seem to be correlated to the in-plane STO axis for the thick film but eventually along [010] and $[0\bar{1}0]$ for the thin film.

Assuming an epitaxial relationship between the film and the substrate, the observed (120) and (002) domains in the PZ films are oriented in plane to minimize the lattice misfit with the substrate as shown for both domains in Fig. 4(a). Note, that the lattice misfit is not visible in this schematic figure. Depending on the orientations of the in-plane components, different variants for each of these two domains can occur as shown in the cross section views in Fig. 4(b). There are four main variants for the (120) domains, Figs. $4(b)_1$–$4(b)_4$, and two main variants for the (002) domains, Figs. $4(b)_5$–$4(b)_6$.

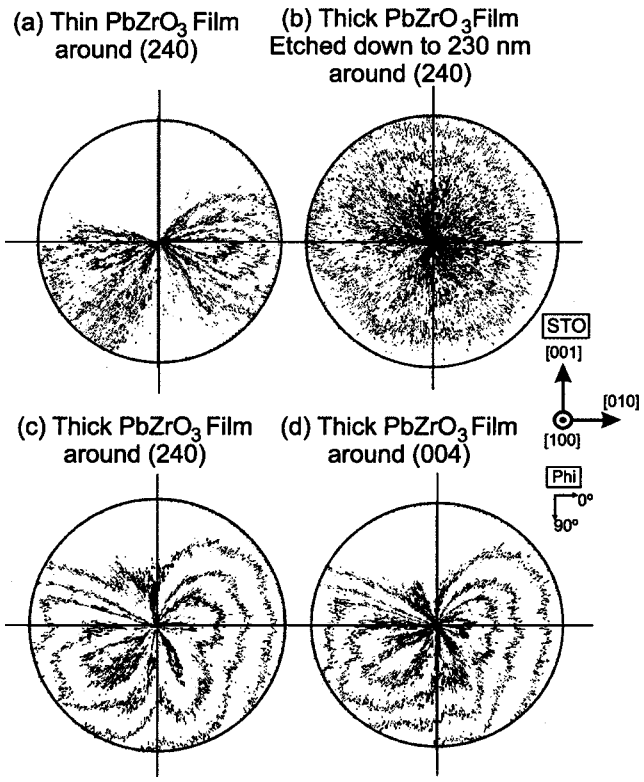

FIG. 3. (a–c) Pole figures around the symmetric (240) peak in the PZ films and (d) around the symmetric (004) peak in the thick $PbZrO_3$ film. For a pole figure, a phi scan is performed in the θ–2θ diffraction condition of the peak for different chi values (0° to 3° for all pole figures shown here).

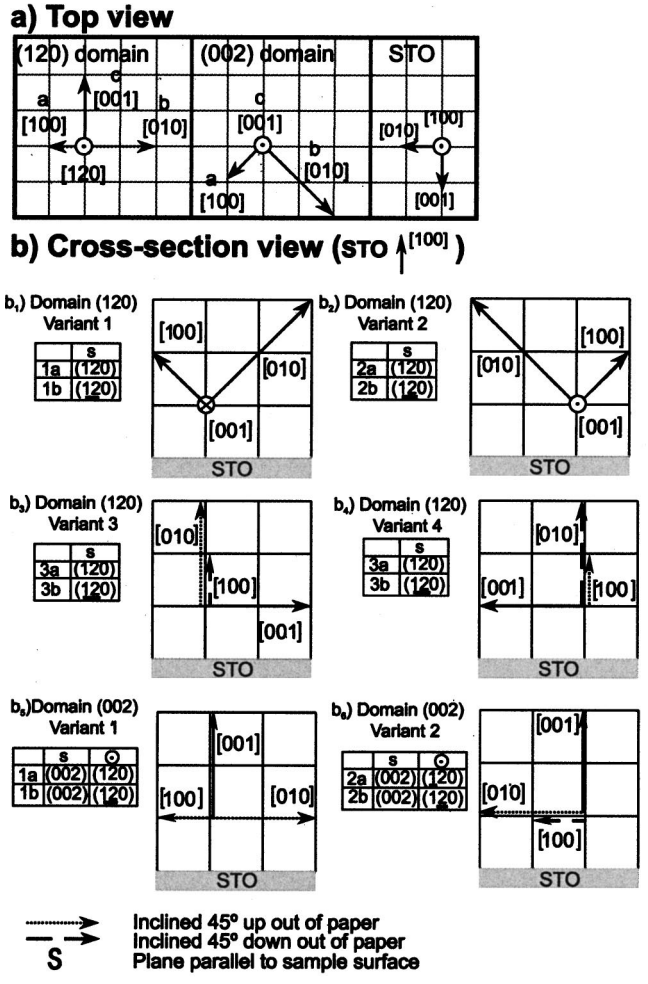

FIG. 4. Schematic representations of the epitaxial relations between the orthorhombic PZ unit cell (vectors) and cubic STO. For both top and cross section views, the STO orientation is given. Dotted and dashed lines represent vectors pointing 45° respectively out and in the paper. (a) Representation of (120) and (002) domains in top view and (b) representation of the different possible variants for each domain in cross section view. The first variant of each domain corresponds directly to the top view.

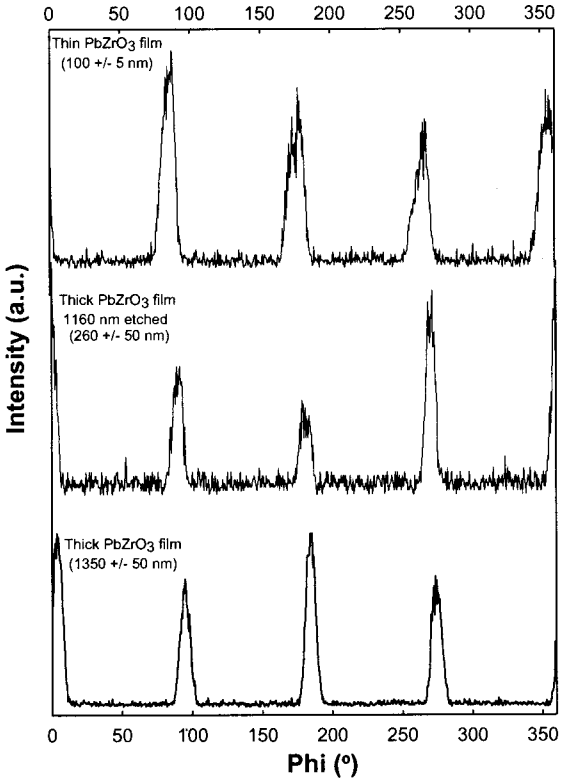

FIG. 5. Phi scan around the asymmetric (362) peak of the (120) domain for the thin PZ film, the thick PZ film etched down to 260 nm, and for a thick PZ film.

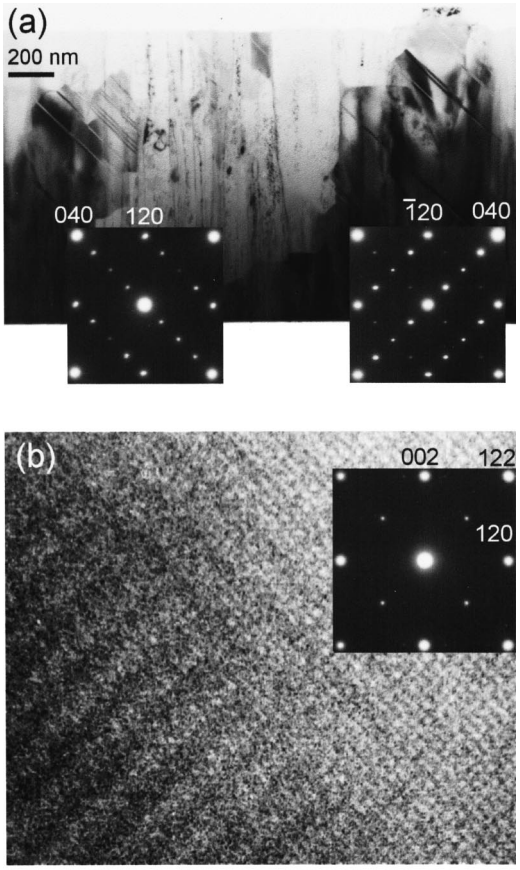

FIG. 6. (a) BF transmission electron micrograph of the PZ layer imaged with a 040 reflection in the dark regions. Light and dark areas correspond to different variants in the layer, as demonstrated by the inserted SADP. They were taken from the corresponding areas after tilting the specimen about 20° to the [001] beam direction. Note that in the right-hand side SADP, a variant with the *b* axis in the plane of paper inclined to the left-hand side is also partly present. (b) HREM image of the PZ layer showing three different variants. The surface normal is directed in the vertical direction of the figure. The two variants with the *b* axis in the plane of the paper are recognized from the 11.8 Å spacing, present in two directions in two different areas, respectively. A variant with the *b* axis inclined to the image plane can be seen in the right-hand side part of the image. A SADP from such an area is inserted. Note that the SADP is consistent with different variants, for example as indexed, but an indexing with a (120) plane parallel to the surface is also possible.

All the variants are composed of two subvariants leading to a total of 12 possibilities. In Fig. 5, x-ray phi scans performed around the asymmetric (362) peak of the (120) domains are shown. The scans for the thin and thick PZ films are similar and show peaks at phi=0 and 180° corresponding to variant 1 and/or 2 and peaks at phi=90 and 270° corresponding to variant 3 and/or 4. This indicates that two variants of the (120) domain are present in the thick as well as in the thin films.

The occurrence of different domain variants was confirmed by cross section analyses of a thick PZ film by TEM. A general overview of the cross section is given in Fig. 6. Selected area diffraction patterns (SADP) and high-resolution electron microscopy (HREM) images were analyzed to differentiate one variant from another. By checking if the *b* axis (for PZ) was in the plane of the SADP, and the lattice plane spacing values in the SADP plane, differentiation between the variants was possible. Within the limited sample volume addressed by TEM, (120) domain variants 1 and 2 occurred most frequently and very few of the other variants were observed. High electron-dose exposure caused a frontlike boundary to move from the edge of the specimens toward the thicker foil areas indicating that the variants are beam sensitive. In one area, diffraction on both sides of the growth front showed that variants with the *b* axis out of the image plane ((120) for variants 3 or 4, and/or (002) for variants 1 or 2) were growing at the expense of (120) variants 1 or 2 (*b* axis in the image plane). The *d*-spacing values of the (120) and (002) planes are in agreement with XRD measurements, as can be seen in Table IV. The *d*-spacing values of the thick PZ films obtained directly from the 2θ spectra were confirmed by the Bond technique at two opposite incidence angles to eliminate instrumental errors. Table IV shows that, within the experimental error, the measured *d*-spacing values

TABLE IV. *d*-spacing values of (120) and (002) planes determined by SADP (TEM) and XRD, and compared to powder PZ.[a]

	d(120) (Å)	*d*(002) (Å)	*d*(240) (Å)	*d*(004) (Å)
TEM-thick Film (±0.4)	4.19	4.14	⋯	⋯
XRD-thick film (±0.005)	4.15/4.16	4.11/4.12	2.07/2.09	2.05/2.06
XRD-thin film (±0.01)	4.17	⋯	2.09	⋯
Powder[a]	4.16	4.11	2.08	2.06

[a]See Ref. 19.

correspond well to powder PZ data.[19] The peak splitting observed in the XRD spectra could not be observed in the SADP's since, with an instrumental error of ~1%, the selected area diffraction technique is less sensitive than XRD.

In the XRD-crystallographic reference,[19] the intensity ratio of $I(120)/I(002)$ and $I(240)/I(004)$ for a random PZ powder are stated to be 1.50 and 1.75, respectively. On the other hand, the XRD spectrum in Fig. 2(b) shows similar intensities for both the (120) and (002) related peaks. It therefore indicates that a majority of (002) domains is present, which is in contrast with the TEM analysis, indicating a majority of (120) domains. As the etch experiments show that the majority of the (002) domains is present in the upper 600 nm of the layer, the larger (002) domain percentage detected by XRD can be explained by its depth sensitivity. For PZ, with an x-ray absorption factor of ~3600 cm^{-1}, the XRD peak intensity is three times stronger at the surface of the material than at a depth of 550–600 nm.[20]

In agreement with the present findings, a single crystallographic domain film has been reported by Bai *et al.*[21] for 100–200 nm thick MOCVD PZ films on STO, analyzed by XRD and TEM measurements. However, in contrast to the present work, they define their layer, which shows two peaks at $2\theta = 21.5°$ and 43.8° in the θ–2θ XRD spectrum, as being (002) oriented. Based on the additional information just presented, we tend to believe that this is an incorrect assignment. Foster *et al.*[16] report on MOCVD grown 500–1200 thick PZ films on STO. Their films have two main orientations in the XRD at roughly $2\theta = 43.5°$ and 44.1° attributed, respectively, to (240) and (004). The additional splitting from the (240) and (004) was further attributed to Cu $K\alpha_1$ and $K\alpha_2$. The peak positions match the ones of our films as listed in Table III. Our peak splitting, however, can not be due to Cu $K\alpha_1$ and $K\alpha_2$ splitting as the maximum 2θ spacing is higher by 0.1° than would be expected between Cu $K\alpha_1$ and $K\alpha_2$ for $2\theta = 43.5°$. Additionally, the pole figures recorded with a monochromator confirmed that both (120) and (002) related peaks were tilted. The main origin of the peak splitting of both (240) and (004) (or tilting) is likely due to the mosaic structure of the substrate described herein. However, domain tilting might be expected in the (120) domains of a PZ film grown on a perfect STO substrate. In the room-temperature PZ structure, the (120) planes are not completely parallel to the substrate. The normal of the (120) planes is tilted by 5′28″, with respect to the STO substrate surface, due to the stretch leading to the orthorhombic structure (Fig. 1). The stretching in different directions corresponding to the formation of the different (120) domain variants is therefore expected to result in peak splitting. But the tilt results in a maximal 2θ difference of $4 \times 5'28'' = 0.3644°$, larger than the maximal measured 2θ difference 0.28° for (240) (Table III). Additionally, it was reported in literature, that the tilts of (200) and (002) domains in PT films increased when relatively slow cooling rates were used after growth.[22] In our work, the noncontrolled cooling rate of ~25 °C/min from 700 °C to 300 °C and of ~3 °C min from 300 °C to room temperature might be compared to the standard (30 °C/min) and slow (5 °C/min) cooling rates as used by Foster *et al.*[22] Therefore, the tilt of the (120) domains might be influenced in a similar fashion as reported by Foster *et al.*[22]

The STO–PZ interface was studied using cross section TEM analyses. The PZ composition did not vary at the interface but a highly defective zone of roughly 10 nm thickness was identified. Voids and misfit dislocations were detected in this zone by, respectively, taking bright-field (BF) electron micrographs in underfocus and by tilting the sample position. Additionally, threading dislocations extending from the interface to the sample surface are observed in most of the micrographs. A threading dislocation density on the order of 10^{10} cm^{-2} was estimated using a TEM foil-specimen thickness of 0.1 μm. This dislocation density is comparable to the threading dislocation density of 10^9–10^{10} cm^{-2} observed by top view TEM for a PT film grown on MgO.[11] PT films on MgO have similarities with PZ films on STO as they grow with a relatively high lattice mismatch (6.8% at 700 °C) and go through a phase transformation upon cooling.

D. Morphology

The as-grown thick PZ film surfaces are peculiar. They consist of a flat surface partly covered with pyramidal structures, all oriented in the same fashion with respect to the substrate, as shown in the SEM photo in Fig. 7(a). It is possible to distinguish fully grown well-shaped pyramids with similar lateral dimensions and an average height of about 250 nm. In some areas, appearing opaque to the naked eye, the film surface was fully covered with pyramids [Fig. 7(b)]. The pyramids in these areas are significantly smaller and usually irregularly shaped as they hamper each other's development or grow together as shown in Figs. 7(b) and 7(c). Occasionally, flat square crystals, rotated 45° in plane with respect to the pyramids, were observed next to or below the pyramids as shown in Fig. 7(d). The side facets of the pyramids have an inclination of about 50° with the substrate surface, as shown in the crystal drawings in Fig. 7 displaying the angles, determined using AFM, between the facets of the pyramids and the surface of the film. The morphologies of the thin film and the etched thick film, observed by AFM, did not display specific features. The roughness, root-mean-square (rms), of the successively etched film was reduced from 30–50 nm to around 20 nm, due to the disappearance of the pyramids. The thin PZ film has a rms below 1 nm.

As both the second-crystallographic domain and the pyramids were exclusively found on the thick films, one might speculate that these two features are correlated. The pyramids might eventually be outgrowths from the (002) domains. To check this assumption, local XRD θ–2θ measurements were performed in zones with a high pyramid density and in zones with a low pyramid density. However, no difference in the XRD intensity ratios of (120) and (002) peaks was observed. Figure 8(a) shows that the pyramids are easily observed in cross section TEM photographs. The detailed photograph in Fig. 8(b) shows a typical V-shaped area under the pyramids. However, for the area shown in Fig. 8(b), no differences in crystallographic domains were observed between the V-shaped zone and directly adjacent areas. Only variant 1, corresponding to (120) domain, was observed.

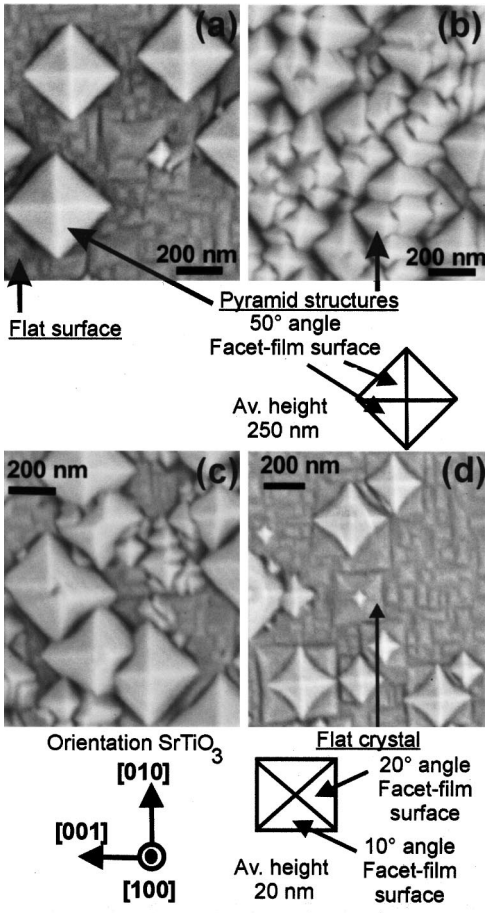

FIG. 7. SEM photos and schematic representations of the surface morphologies of the PZ films on STO substrates. (a) SEM photo of a PZ surface partly covered with pyramids, (b) SEM photo of a PZ surface densely covered with pyramids, (c) details of a SEM photo showing coalescent pyramids, and (d) SEM photo of the PZ surface displaying superposition of a pyramid on a square crystal. The schematic representation of the pyramid and the flat crystal are based on AFM data.

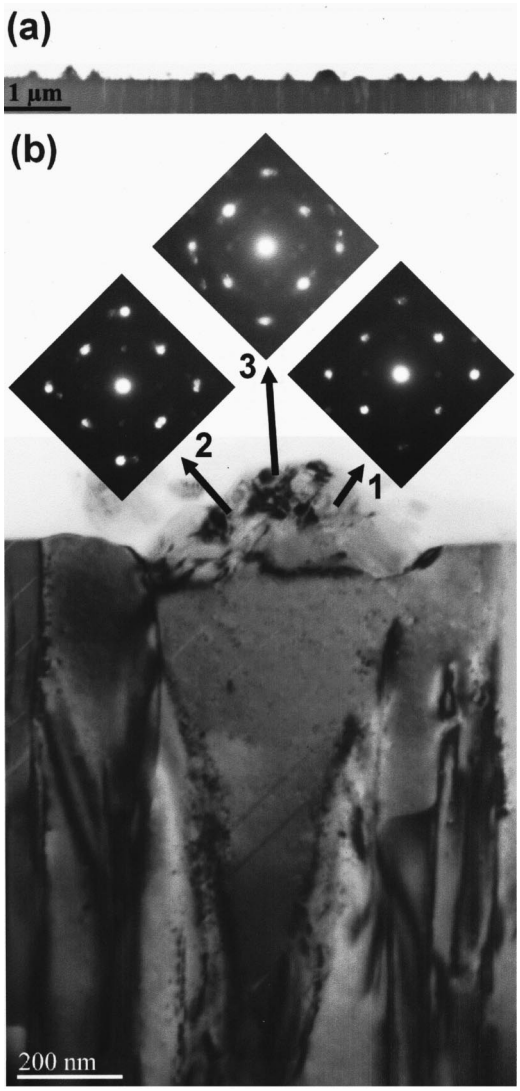

FIG. 8. Cross section transmission electron micrographs of a PZ film on STO. (a) The pyramids seen at the top of the surface correspond to those observed at the surface in top view by SEM. (b) Detailed cross section of a pyramid with the typical V-shaped area observed under the pyramid. The inserted CBED of area 2 shows that at least two variants are present therein.

Compared to the rest of the layer, the V-shaped area has a higher density of dislocation loops, as shown in Fig. 9. Furthermore, large voids, confirmed in under and over focus experiments, were found around the V-shapes. Enlargements of the pyramid areas reveal that about half of them do not have a uniform structure. For example, the pyramid imaged in Fig. 8(b) is built up in layers. Local electron diffraction analyses on different locations in the pyramid itself, using convergent beam electron diffraction (CBED) with a probe of 20 nm, indicate that slightly different orientations are present in the pyramids as is shown in Fig. 8(b). The CBED analyses reveal a weak and a strong pattern in area 2 of Fig. 8(b). The patterns are mutually tilted by 5° and have slightly different *d* spacing normal to the surface (4.15 Å and 4.10 Å) indicating the formation of local (002) domains at the top of the pyramid.

The results described herein indicate that the pyramids are certainly not originating exclusively from (002) domains. Using a crystal morphology editor/viewer,[23] it is possible to simulate (002) or (120) textured pyramids with ~50° inclined low indices planes, corresponding to the SEM and AFM observations. In Figs. 10(b) and 10(d), it is shown that fully developed pyramids are obtained if the growth rate of the (120) and (002) top facets is at least 1.8 times larger than that of the pyramid side facets. An eventual facet indexing for the pyramids, based on the in-plane orientation of PZ on

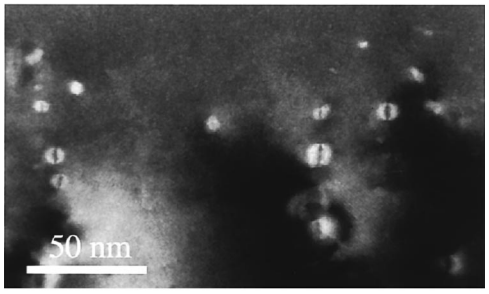

FIG. 9. BF transmission electron micrograph of the typical dislocation loops observed in the V-shaped area located under the pyramid.

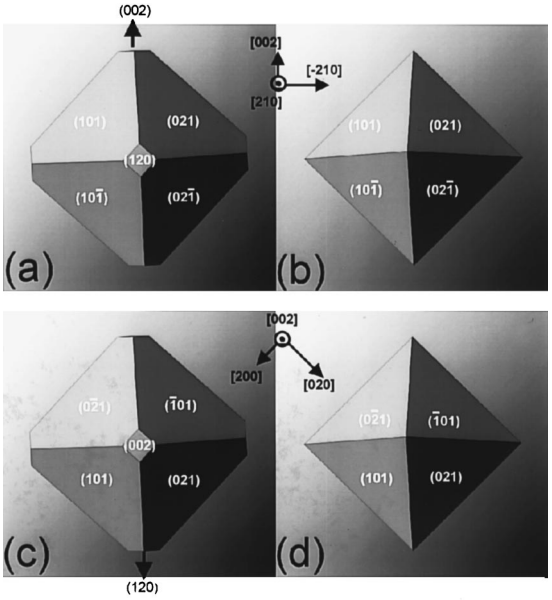

FIG. 10. Simulated crystal shapes using a crystal morphology editor and viewer (see Ref. 23) to visualize the pyramids. (a) Pyramid issued from a (120) domain with a {120} and {002} growth rate of 1.5, (b) Pyramid issued from a (120) domain with a {120} and {002} growth rate of 1.8, (c) Pyramid issued from a (002) domain with a {120} and {002} growth rate of 1.5, and (d) Pyramid issued from a (002) domain with a {120} and {002} growth rate of 1.8.

STO and the angles in between the facets measured by AFM, is given in Fig. 10. The angles of roughly 54° between the indexed facets (Table V) correspond well to the 50° angle observed by AFM (Fig. 7). The facets of the pyramids originating from (120) or (002) domains are the same but occur in a different order. It comes from the fact that there is only a rotation of 90° around the $[\bar{2}10]$ axis between an (002) oriented pyramid and (120) oriented one, and vice versa, as can be seen in Figs. 1 and 10. The occasionally observed square flat crystals might result from different growth rates from other facets leading to different squarelike flat pyramids.

E. Discussion

At 700 °C, cubic PZ grows epitaxially on cubic STO crystal. As shown in Fig. 1, upon cooling, cubic PZ is deformed to an orthorhombic PZ structure by stretching the cubic structure along one of its 12 edges, i.e., along one of the ⟨110⟩ directions. These 12 deformation possibilities result in a maximum of six different geometries of the PZ structure with respect to the STO substrate [see Fig. 4(b)]. For a stretch along $[1\bar{1}0]$, as shown in Fig. 1, the thin-film–substrate relation is, by using pseudocubic notation for the PZ structure, (100)[010]PZ//(100)[010]STO corresponding to (120)[002]PZ//(100)[00$\bar{1}$]STO using the orthorhombic notation. However, the thin PZ film obtained in the present study shows the presence of several (120) domain variants. This means that the elongation has occurred along several out-of-plane ⟨110⟩ directions of the pseudocubic structure, namely $[1\bar{1}0]$, [110], [101], and, $[10\bar{1}]$, corresponding, respectively, to variants, 1, 2, 3, and 4 of (120) domains. Stretching along the four other out-of-plane $[\bar{1}10]$, $[\bar{1}\bar{1}0]$, $[\bar{1}01]$, $[\bar{1}0\bar{1}]$ directions is physically identical to stretching along $[1\bar{1}0]$, [110], [101], and, $[10\bar{1}]$, leading to an $(\bar{1}\bar{2}0)$ oriented domain instead of a (120) domain. Therefore, these variants are not actually different variants and are called subvariants as shown in Fig. 4(b). At room temperature, the thin PZ film is not hetero-epitaxial as there is an orthorhombic structure on a cubic structure and the film contains one crystallographic domain composed of a maximum of four variants. The film is therefore not epitaxial in the way it is usually mentioned in the context of III–V materials,[24] but possesses much more than a local epitaxy, therefore, we define the film as semi-epitaxial.

TABLE V. Angles between the facets as calculated with a crystal morphology editor/viewer.[a]

	(120)	(002)
(101)	54.9	54.4
(021)	54.9	54.4

[a]See Ref. 23.

The structure of PZ films thicker than ~260 nm deviates even more from an epitaxial structure since (002) domains are formed in addition to (120) domains. It is clear that above the threshold thickness (~260 nm), the impact of the STO substrate on film orientation is less and the cubic structure can be stretched along the in-plane ⟨011⟩ directions leading to (002) domains. Referring to Fig. 4(b), a stretch along $[0\bar{1}1]$ and [011] leads, respectively, to (002) domain variants 1 and 2. For a stretch along $[0\bar{1}\bar{1}]$ the thin-film–substrate relation is, using pseudocubic notation for the PZ structure, (00$\bar{1}$) [010]PZ//(100)[010]STO corresponding to (002)[100] PZ//(100)[011]STO using the orthorhombic notation. Elongations along $[01\bar{1}]$ and $[0\bar{1}\bar{1}]$ are directly equivalent leading to the subvariants of (002) domains, just as for the (120) domains. In fact, an (002) domain corresponds simply to a (120) domain rotated by 90° from in and out of plane, as can be seen in Figs. 1 and 4(a). The relation between the (120) and (002) domains is clearly seen with the pyramids at the sample surface, which can originate from both types of domains. Figure 10 shows that, if an (120) oriented pyramid is rotated by 90° around the $[\bar{2}10]$ axis, such that the [002] orientation becomes normal to the surface, it becomes an (002) oriented pyramid. Pyramids from both (120) domain variant 1 and (002) domain variant 1 have the $(1\bar{2}0)$ or $(\bar{1}20)$ side planes in common as can be seen in Fig. 10. The development of pyramids at the PZ surface is due to a locally higher growth rate of the (120) and (002) planes with respect to the pyramid facets and to the (120) and (002) planes of the surrounding flat surface domains. Initially, the higher growth rate might be triggered by some kind of defect, and then it grows out as a V shape. The V-shaped area under the pyramid contains a higher density of dislocation loops than the adjacent areas. Since growth of the V-shaped crystal volumes did not proceed along {120} and {002} planes, as for the rest of the layer, but took place through the {101} and {021} side facets of the pyramids, this might result in a different defect level with respect to the rest

TABLE VI. Mismatch and thermal strain in PZ films on STO substrates as a function of temperatures. Mismatch: $f=(a_{STO}-a_{PZ})/a_{PZ}$ above T_c and as described in Eqs. (1) and (2) for temperature lower than T_c. Thermal strain: $\epsilon_T=(\alpha_{STO}-\alpha_{PZ})\Delta T$.

Temp[b] (°C)	PZ lattice constants (Å)	PZ thermal expansion coefficient (10^{-6} K^{-1})	STO lattice constants (Å)	STO thermal expansion coefficient (10^{-6} K^{-1})[c]	Mismatch f (%)
700	4.161	7.7[c]	3.934	11.7	−5.5
500	4.155	7.7[c]	3.925	11.2	−5.5
230 ($\approx T_c$)	4.146[e]	7.7[c]	3.913	10.4	−5.6
150	$a\approx5.87$ $b\approx11.73$ $c\approx8.24$	−0.5 (a′,b′)[a,e] 28 (c′)[a,e]	3.910	10.6	−5.1 for (120) up and −5.7 and −5.8 for (002) up
RT[d]	$a=5.884$ $b=11.768$ $c=8.220$	−0.5 (a′,b′)[a,e] 28 (c′)[a,e]	3.905	10.3	−5.0 for (120) up and −6.1 and 6.2 for (002) up

Temperature range	Thermal strain
700–230	$\sim1.6\times10^{-3}$ (compressive upon cooling)
230-RT	along a′, 2.2 10^{-3} (compressive upon cooling) along c′, −3.6 10^{-3} (tensile upon cooling)

[a]The expansion coefficients are given for a′,b′, and c′ being the pseudotetragonal unit cell parameters.
[b]Temp indicates temperature.
[c]See Ref. 25.
[d]RT indicates room temperature.
[e]See Ref. 18.

of the layer. Alternatively, the higher defect level is expected to result in the increased growth rate of the (120) and (002) top faces of the V-shaped area. The growth rate can be estimated to be 1.2 times higher than in the flat domains, by considering that the largest pyramids have a height of roughly 250 nm and that the largest pyramids start roughly at the threshold thickness of 260 nm for a ~1400 nm thick PZ layer. This higher growth rate of the (120) and (002) in the pyramids might be a contributing factor to the 2.5 larger growth rate of the thick films with respect to the thin films (Table II) as the thick films contain many pyramids. Nevertheless, the major factor for the higher growth rate of the thick film is that the PZ layer seems to grow faster once the substrate is covered by PZ as we observed a similar behavior for the other PZT compositions grown.

The room-temperature lattice mismatch (f) for (120) oriented domains is determined by

$$f(120)=\frac{2a_{STO}-c_{PZ}}{c_{PZ}}=-5.0\%, \quad (1)$$

and the lattice mismatch for the (002) oriented domains is determined by

$$f(002)\ \text{ along }\ [010]=\frac{2\sqrt{2}a_{STO}-b_{PZ}}{b_{PZ}}=-6.1\%, \quad (2a)$$

$$f(002)\ \text{ along }\ [100]=\frac{\sqrt{2}a_{STO}-a_{PZ}}{a_{PZ}}=-6.2\%. \quad (2b)$$

For both domains, the calculated lattice mismatch at room temperature indicates a PZ film in compression. Nevertheless, the 2θ peaks observed in the XRD spectra of Fig. 2(b) and listed in Table III indicate that only the thin film is under compressive stress with the $d(120)$ lattice planes 0.2% in tensile stress. As can be seen in Table VI, the lattice mismatch is roughly constant at all temperatures. It is expected that most of the lattice mismatch is absorbed in the defective intermediate layer of roughly 10 nm observed at the STO–PZ interface which contains numerous misfit dislocations and voids. Additionally, the threading dislocations, observable in most BF micrographs, originate from this layer. Their presence might be correlated to misfit dislocations and stress release.[24] Nevertheless, additional minor factors also contribute to stress release as no stress is observed in the thick layers. The formation of all possible domain variants above the threshold thickness might be one of these minor factors. The thermal expansion coefficient[25] difference between STO and PZ is not large with respect to the lattice misfit, therefore, as can be seen in Table VI, its role is minor. But below the Curie temperature, the expansion coefficient along the pseudocubic c axis is 28×10^{-6} K^{-1} and -0.5×10^{-6} K^{-1} along the two other axes,[18] therefore, when the c axis is in plane, as for (120) domains, tensile stress will develop that might compensate for compressive mismatch stress.

IV. SUMMARY

The structure and the morphology of PZ films grown on STO by MOCVD have been investigated. A schematic overview of the important observed features is shown in Fig. 11. At 700 °C, the PZ films are epitaxially grown in their cubic paraelectric phase on cubic STO substrates. During cool down, the cubic PZ structure is transformed to orthorhombic as it goes through the paraelectric–AFE phase transition. For a film thinner than the threshold thickness of ~260 nm, the stretching of the cubic structure responsible of the ortho-

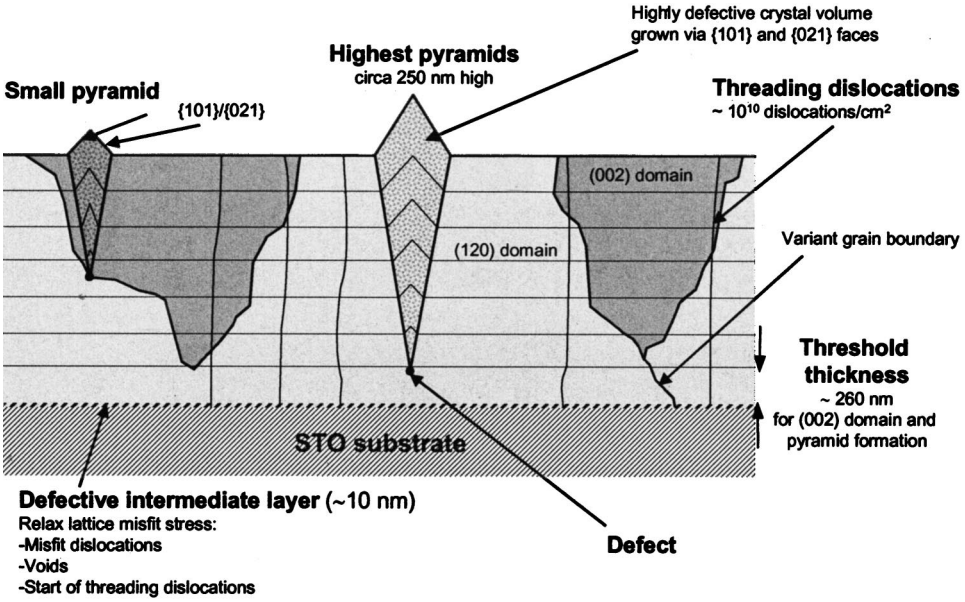

FIG. 11. Schematic cross section of a thick PZ film detailing the different features of these films as observed and discussed in the present work.

rhombic structure is limited to four pseudocubic directions [110], $[1\bar{1}0]$, [101], and $[10\bar{1}]$ and results in a semi-epitaxial PZ film composed of a maximum of four (120) domain variants. For films thicker than the threshold thickness, the stretching of the cubic structure can also occur along the $[0\bar{1}1]$ and [011] directions due to the reduced impact of the substrate. The resulting PZ layer is composed of (002) as well as (120) oriented domains with, respectively, 2 and 4 variants each. These variants correspond to the six different elongation directions (along the 12 cube edges from the cube) of the paraelectric cubic structure to form the AFE orthorhombic structure. The lattice misfit is roughly -5% at all temperatures, but only the 100 nm thick PZ layer is in slight compression. At the interface STO–PZ, a layer of roughly 10 nm thickness, containing voids, misfit dislocations, and the origins of the threading dislocations growing up to the film surface, was observed. The defective intermediate layer formation and its associated mechanisms probably accommodate most of the lattice misfit. For layers thicker than the threshold thickness of 260 nm that are relaxed at room temperature, the additional formation of (002) domains might also contribute to release the remaining lattice misfit stress. In addition to (002) domain formation, peculiar pyramids of different sizes are observable at the surface of films thicker than the threshold thickness of $\sim$260 nm. Pyramids can originate from (120) and (002) domains and develop due to a $\sim$1.2 higher growth rate of the {120} and {002} planes in the pyramids with respect to the rest of the layer. Initially, the higher growth rate might be triggered by any kind of defect. The formation of pyramids leads to V-shaped zones growing from {101} and {021} facets containing a high dislocations density with respect to the rest of the layer growing from {120} and {002} planes, indicating eventual differences in the layer growth mechanisms between {101}, {021} and {120}, {002} planes.

ACKNOWLEDGMENTS

This project is supported by STW (Dutch Technology Foundation). Harry van der Linden is acknowledged for the reactive ion etching of the $PbZrO_3$ film and Harrie Jaspers for the XRF measurements.

[1] B. Jaffe, W. R. Cook, and H. Jaffe, *Piezoelectric Ceramics* (Academic, London, 1971).
[2] R. Ramesh, *Thin Film Ferroelectric Materials Devices* (Kluwer, Boston, 1997).
[3] Y. Xu, *Ferroelectric Materials and their Applications* (Elsevier Science, New York, 1991).
[4] G. H. Haertling, Ferroelectrics **75**, 25 (1987).
[5] K. Yamakawa, S. Trolier-McKinstry, J. P. Dougherty, and S. B. Krupanidhi, Appl. Phys. Lett. **67**, 2014 (1995).
[6] H. Maitwa and N. Ichinose, Jpn. J. Appl. Phys., Part 1 **40**, 5507 (2001).
[7] F. Wang, K. K. Li, and G. Haertling, Appl. Phys. Lett. **65**, 2507 (1994).
[8] K. S. Lee, J. H. Choi, J. Y. Lee, and S. Baik, J. Appl. Phys. **90**, 4095 (2001).
[9] V. Nagarajan, C. S. Ganpule, H. Li, L. Salamanca-Riba, A. L. Roytburd, E. D. Williams, and R. Ramesh, Appl. Phys. Lett. **79**, 2805 (2001).
[10] A. L. Roytburd, S. P. Alpay, L. A. Bendersky, V. Nagarajan, and R. Ramesh, J. Appl. Phys. **89**, 553 (2001).
[11] C. M. Foster, Z. Li, M. Buckett, D. Miller, P. M. Baldo, L. E. Rehn, G. R. Bai, D. Guo, H. You, and K. L. Merkle, J. Appl. Phys. **78**, 2607 (1995).
[12] S. K. Streiffer, C. B. Parker, A. E. Romanov, M. J. Lefevre, L. Zhao, J. S. Speck, W. Pompe, C. M. Foster, and G. R. Bai, J. Appl. Phys. **83**, 2742 (1998).
[13] A. E. Romanov, M. J. Lefevre, J. S. Speck, W. Pompe, S. K. Streiffer, and C. M. Foster, J. Appl. Phys. **83**, 2754 (1998).
[14] L. Čakare, B. Maličˇ, M. Kosec, and A. Sternberg, Ferroelectrics **241**, 107 (2000).
[15] S. S. N. Bharadwaja and S. B. Krupanidhi, J. Appl. Phys. **86**, 5862 (1999).
[16] C. M. Foster, G.-R. Bai, R. Csencsits, J. Vetrone, R. Jammy, L. A. Wills, E. Carr, and J. Amano, J. Appl. Phys. **81**, 2349 (1997).
[17] M. P. Moret, M. A. C. Devillers, K. Wörhoff, and P. K. Larsen, J. Appl. Phys. **92**, 468 (2002).
[18] T. Mitsui and S. Nomura, in Landolt-Börnstein: *Ferroelectrics and related substances*, Vol. 16, Numerical Data and Functional Relationships in Science and Technology, edited by K.-H. Hellwege, (Springer, Berlin, 1981).
[19] International Centre for Diffraction Data: Card ICSD 75-1607.

[20] B. D. Cullity, *Elements of X-ray Diffraction* (Addison–Wesley, London, 1978).
[21] G. R. Bai, H. L. M. Chang, D. J. Lam, and Y. Gao, Appl. Phys. Lett. **62**, 1754 (1993).
[22] C. M. Foster, W. Pompe, A. C. Daykin, and J. S. Speck, J. Appl. Phys. **79**, 1405 (1996).
[23] Crystal Morphology Editor and Viewer-JCrystal 1.02.
[24] M. Ohring, *The Materials Science of Thin Films* (Academic, Boston, 1992), p. 322.
[25] Y. S. Touloukian, R. K. Kirby, R. E. Taylor, and T. Y. R. Lee, *Thermophysical Properties of Matter: Thermal Expansion Nonmetallic Solids*, Vol. 13 (IFI/Plenum, New York, 1977).